Pure Appl. Geophys. 168 (2011), 827–844

DOI 10.1007/s00024-010-0149-2

Pure and Applied Geophysics

Crustal Configuration of the Northwest Himalaya Based on Modeling of Gravity Data

Ashutosh Chamoli,[1] Anand K. Pandey,[1] V. P. Dimri,[1] and P. Banerjee[2]

Abstract—The gravity response and crustal shortening in the Himalayan belt are modeled in detail for the first time in the NW Himalaya. The Bouguer gravity anomaly along a ~450-km-long (projected) transect from the Sub-Himalaya in the south to the Karakoram fault in the north across the Indus-Tsangpo Suture Zone is modeled using spectral analysis, wavelet transform and forward modeling. The spectral analysis suggests three-layer interfaces in the lithosphere at 68-, 34- and 11-km depths corresponding to the Moho, the Conrad discontinuity and the Himalayan decollement thrust, respectively. The coherence, admittance and cross spectra suggest crustal shortening because of convergence compensated by lithospheric folding at 536- and 178-km wavelength at the Moho and the upper-crustal level. An average effective elastic thickness of around 31 km is calculated using the coherence method. The gravity data are modeled to demarcate intracrustal to subcrustal regional thrust/fault zones. The geometrical constraints of these faults are obtained in the space scale domain using the wavelet transform, showing good correlation with the major tectonic boundaries. The crustal configuration along the transect shows how the Moho depth increases from 45 to 80 km towards the north with the locus of flexure of the Indian crust beneath the Higher Himalayan zone. The combination of forward modeling and wavelet analysis gives insight into the subsurface extent and geometry of regional structures across the NW Himalaya.

Key words: Crustal structure, spectral analysis, gravity anomaly, wavelet transform, Himalaya.

1. Introduction

The Himalayan mountain belt originated as a consequence of the collision along the Indus-Tsangpo Suture Zone and the continued convergence of the Indian plate with the accreted landmass of Eurasia since the Eocene. The convergence led to the tectonic stacking of upper and mid-crustal slabs on the northern margin of the Indian plate along the foreland propagating intracrustal thrusts originating from the basal decollement called the Main Himalayan Thrust. The compression because of convergence and stacking of crustal slabs over the leading edge of the Indian plate led to the flexure in the Indian plate and progressive thickening of the crust towards the north (Lyon-Caen and Molnar, 1983, 1985). The Moho configuration beneath the Himalaya suggests that the flexural rigidity of the crust decreases northward because of thermal and flexural weakening and the locus of tectonic loading lies beneath the Higher Himalaya (Lyon-Caen and Molnar, 1983, 1985; Cattin *et al.*, 2001; Jordan and Watts, 2005; Hetényi *et al.,* 2006; Tiwari *et al.,* 2006). The attempts to constrain the flexural rigidity or effective elastic thickness (EET) in the continental lithosphere, especially in the Himalayan belt, remain highly variable owing to the preference of modeling technique (Burov and Watts, 2006; Hetényi *et al.*, 2006). Jin *et al.* (1994) illustrated the application of spectral analysis of gravity anomaly and topography data to derive the important constraints in explaining the thickening of the crust in the Himalayan-Tibet region. The results suggest lithospheric folding at two distinct wavelengths because of lateral compression. The larger wavelength corresponds to the undulations of the whole lithosphere, and the shorter wavelength folding is superimposed only in the upper crust. In a similar manner, the two wavelengths of folding are also identified in the western Himalaya to show the buckling of the lithosphere (Caporali, 2000). Further, the geometrical parameters of the causative sources can be derived using the wavelet transform (Fedi and Quarta, 1998; Hornby *et al.*, 1999; Sailhac *et al.*, 2000; Chamoli *et al.*, 2006). The subsurface extension of the regional structures can be constrained by

[1] National Geophysical Research Institute (Council of Scientific and Industrial Research), Hyderabad 500007, India. E-mail: chamoli.a@gmail.com

[2] Wadia Institute of Himalayan Geology, Dehradun 248001, India.

the geological observations based on the structural architecture of litho-tectonic units in the Himalayan thrust-fold belt. The integration of the results of spectral analysis, wavelet transform and geological observations can provide realistic constraints in density structure modeling.

Banerjee and Satyaprakash (2003) acquired the gravity data and carried out a preliminary processing along a ~450-km-long transect across the NW Himalaya, from the sub-Himalayan zone to the Karakoram fault across the Indus Tsangpo suture zone (Fig. 1). In the present study, the Bouguer gravity anomaly and topography are modeled along the transect in an attempt to constrain the crustal configuration and density structure across the NW Himalaya using spectral analysis, wavelet transform and forward modeling. The lithospheric folding and the presence of a weak decoupling layer in the NW Himalaya are also investigated using coherence, admittance and cross spectra of the data as suggested in the earlier studies of Tibet and the western Himalaya (Jin *et al.*, 1994; Caporali, 2000). The wavelet analysis delineated the major thrusts, which act as sources of the anomaly. A model of the density structure is presented incorporating the significant results from the receiver function analysis (Rai *et al.*, 2006), retro-deformable cross sections (Searle, 1986; Powers *et al.*, 1998), microseismicity (Thakur *et al.*, 2000), magnetotelluric study (Arora *et al.*, 2007), INDEPTH study (Hauck *et al.*, 1998) and geological observations (Fig. 1b).

2. Tectonic Setting

The leading edge of the Indian plate shows a layered structure beneath the Himalaya. The microseismicity and the occurrence that most of the Himalayan earthquakes are confined within the upper crust suggest a brittle to brittle-ductile regime of deformation above the Main Himalayan Thrust. The Indian lower crust below the decollement largely remains seismically inactive. The Moho shows flexural buckling with increasing depth towards the north (Lyon-Caen and Molnar, 1983, 1985). This tectonic setup marks a jelly-sandwich type model (Jin *et al.*, 1994; Burov and Diament, 1995; Burov and Watts, 2006) for the leading edge of the Indian plate. The tectonic loading and its isostatic response are reflected in the form of the Himalayan topography, which varies from ~300 to 5,000 m from south to north. The Sub-Himalaya in the south (Fig. 1b) has an average topography of ~1,000 m and is constituted of low-density Neogene sediments of the foreland basin. The height gradually increases to ~3,000 m in the Lesser Himalaya and reaches ~5,000 m beyond the Main Central Thrust-I zone towards the north. The Lesser Himalaya is constituted of mid-late Proterozoic parautochthonous basement and crystalline nappe. The Main Central Thrust-III and -II are variously described as mid-crustal footwall imbricates of the Main Central Thrust-I (Valdiya, 1980; Thakur, 1992; Srikantia and Bhargava, 1998). The marine sediments of the Tethys Himalaya lie to the north of the Higher Himalayan crystallines. These crystallines extend further northwards beneath Tethyan sediments and are exposed in the form of domal upwarp as eclogite bearing Tso Morari crystalline complex (Fig. 1b; Thakur, 1992). The Tethyan sediments juxtapose the rocks of the Indus Tsangpo Suture Zone, which extends up to the island-arc suite of Ladakh batholith. Further north lie the volcanic and sedimentary suites of the Shyok Suture Zone and Karakoram batholith. The representative densities of different litho-tectonic units (Table 1) are used to model the gravity anomaly.

3. Gravity Data

The gravity values were measured using three gravity meters, Scintrex CG3M, Lacoste Romberg and a Sodin gravity meter with an overall accuracy of 0.1 mgal. The station interval ranges from 1.5 to 2 km, except across the Ladakh batholith where it varies from 500 m to 1 km. The accuracy of the leveling survey is of the order of 1 m, which is equivalent to 0.3 mgal in the gravity measurement. This is within the noise level of the Himalayan terrain. The detail of the data acquisition is discussed by Banerjee and Satyaprakash (2003). The measured gravity data are corrected by applying free air and terrain correction up to 170 km. The Bouguer anomaly value varies between −150 and −530 mgal

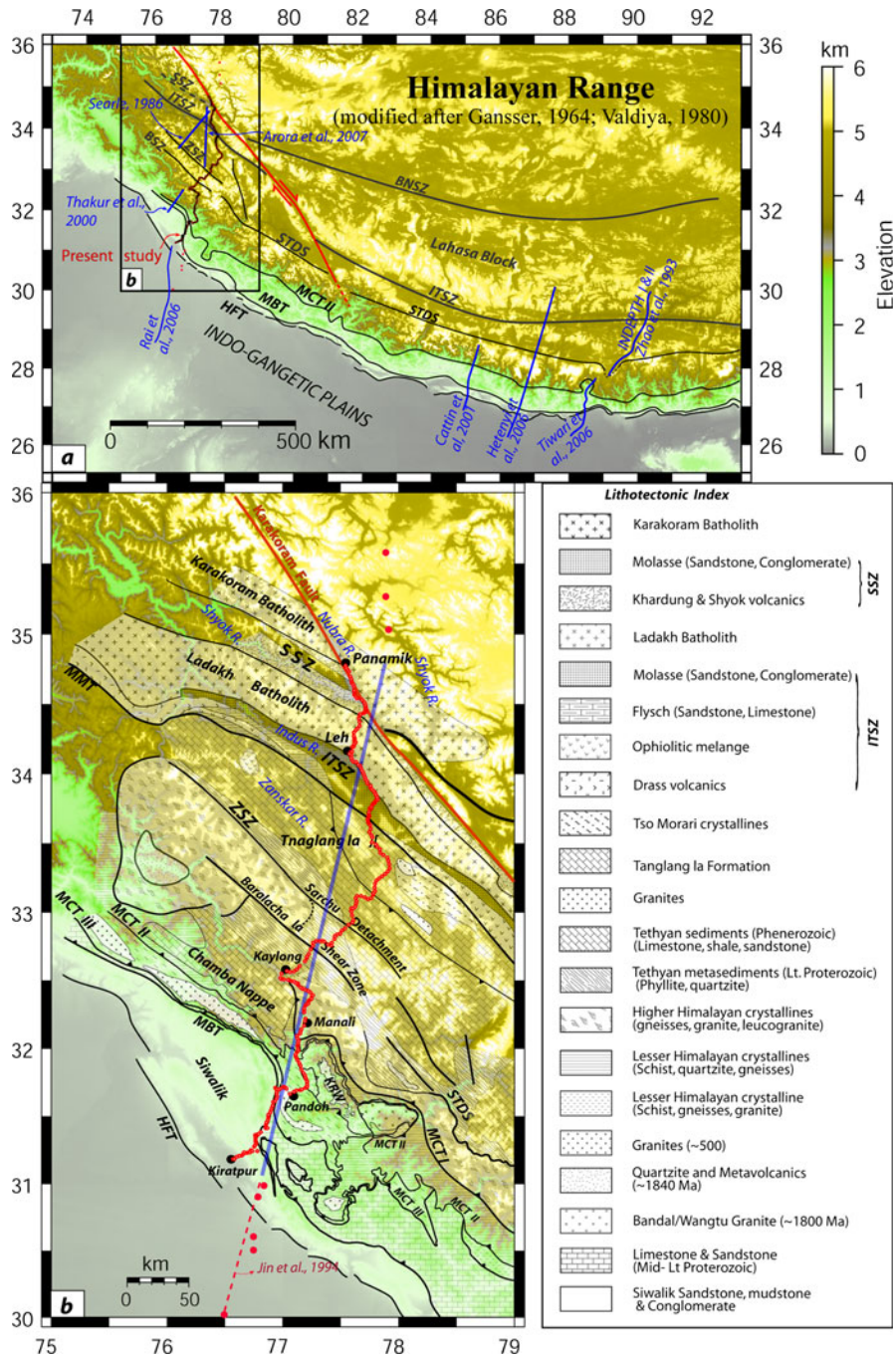

Figure 1

a Tectonic map of the Himalaya showing principal structural element (modified after Gansser, 1964; Valdiya, 1980). **b** Geological map of the NW Himalaya overlaid with studied gravity profile (Kiratpur-Manali-Leh-Panamik) [compiled and modified from Thakur (1992), Srikantia and Bhargava (1998), Pandey *et al.* (2004) and our own observations]. The data points to the south and north of the present profile are derived from Bouguer anomaly contours of Jin *et al.* (1994). The *thick blue line* indicates projected profile. *HFT* Himalayan Frontal Thrust, *MBT* Main Boundary Thrust, *MCT* Main Central Thrust, *STDS* South Tibetan Detachment System, *BSZ* Baralacha la Shear Zone, *ZSZ* Zanskar Shear Zone, *ITSZ* Indus Tsangpo Suture Zone, *SSZ* Shyok Suture Zone, *KRW* Kulu-Rampur window

Table 1

The lithotectonic units with their characteristics lithology and density (g/cm^3) along the profile

Litho-tectonic unit (south-north)	Bulk lithology	Density (observed)	Bulk density (assigned)	Remark
Siwalik group (Neogene)	Sanstone, Mudstone	–	2.6	
Lower tertiary	Limestone, Shale			
Shali group (mid-Lt.Proterozoic)	Limestone Quartzite	2.21–2.84	2.6	
Lesser Himalayan basement (~1,800 Ma)	Granite Gneisses		2.78	
	Quartzite Metavolcanics		2.8	
MCT-II (Jutogh/Munsiari thrust)				
Lesser Himalayan crystallines	Stau.-Garnet schist Quartzite, Gneisses	2.52–2.82	2.6	
	Granite (~500 Ma)			
MCT-I (Vaikrita Thrust)				
Higher Himalayan Crystallines	Ky/Sill Gneiss Banded Gneiss Leucogranite	2.52–2.82	2.70	
STD? (not well defined along the profile)				
(Lt. Proterozoic)	Metasediments Quartzite,	2.47–2.76	2.57	
Tethys Himalaya	Phyllite, Granite (~500 Ma?)			
(Phenerozoic)	Limestone, Shale, Sandstone		2.54	Highly sheared
	Tsomorari crystallines		2.70	Granite gneiss and eclogite lenses
Indus Tsangpo suture zone (ITSZ)	Volcanics, Flysch, Molasses, Ophiolitic mélange	2.70–2.90	2.71	Highly sheared
Ladakh Batholith	Granite, Granitoids	2.57–2.77	2.78	
Shyok Suture zone	Shyok & Khardung Volcanics, Molasses	–	2.6	Highly sheared
Karakoram Batholith	Granite	–	2.77	
Crustal basement			2.78	
Lower crust			2.90	
Mantle			3.30	

along the profile (Banerjee and Satyaprakash 2003). Three distinct zones can be differentiated on the basis of variations in the average gradient of the Bouguer anomaly (Fig. 2). The southern Kiratpur-Manali section, covering the parts of the Sub-Himalaya, Lesser Himalayan parautochthons and crystallines shows an average gradient of 0.8 mgal/km (Fig. 2). The steepest gradient of 1.5 mgal/km is observed between the Keylong-Pang section occupying the Phenerozoic sedimentary sequence of the Tethys Himalaya. Subsequently, the gradient becomes very small with two high-gravity zones corresponding to the Indus Tsangpo suture zone and the Ladakh Batholith, respectively. The northern part of the profile between Khardung and Panamic does not show much variation. The survey limitation is the traverse along the river valleys that causes unavoidable strike parallel observations. Thus, the 580-km-long traverse is projected to a ~450-km-long profile (Fig. 1b) largely across the Himalayan belt. The Bouguer anomaly values from the Gangetic plane along the profile are added from Jin *et al.* (1994) to get a better constraint on the Moho geometry of the underthrusting Indian plate at the Himalayan front and to overcome the immediate edge effects in the modeling.

3.1. Spectral Analysis

Bouguer anomaly and topography along the transect are analyzed by different spectral methods. The power spectrum of Bouguer anomaly is calculated to derive the mean depth of the interfaces. The coherence function is calculated and interpreted to derive the EET and configuration of relative folding of the crustal layers. The admittance and cross spectra are calculated and correlated to understand the folding of the layers and the presence of a

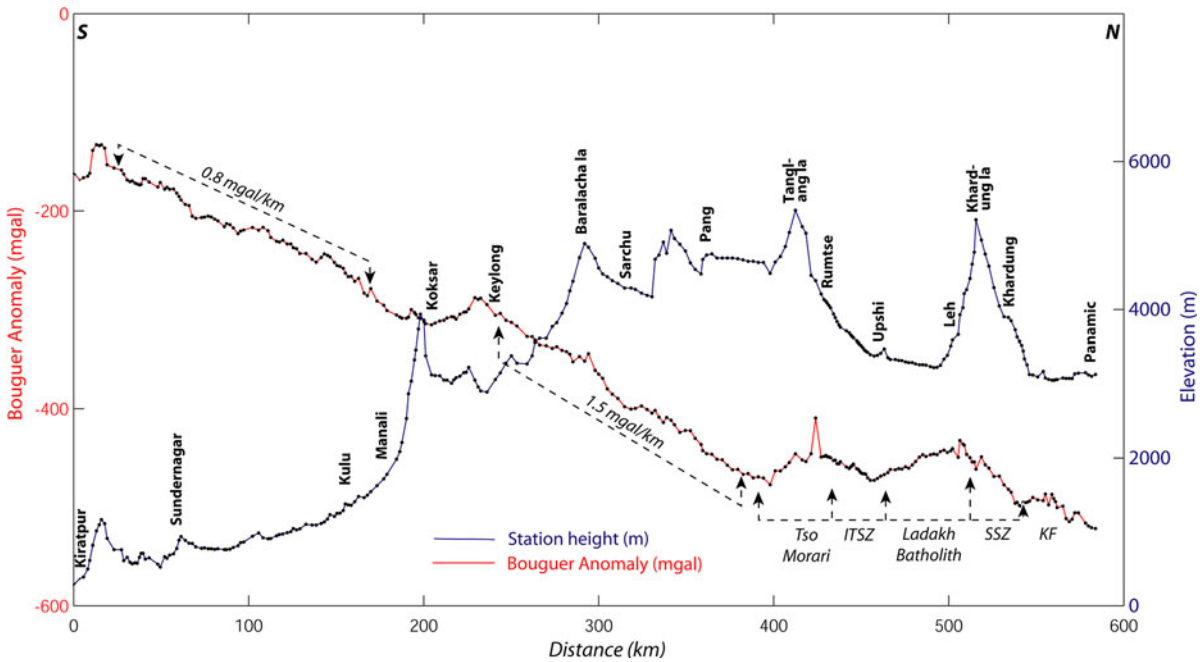

Figure 2
Observed Bouguer gravity anomaly and station elevation along the Kiratpur-Manali-Leh-Panamic profile across the NW Himalaya. Note the segments of the profile with different average gradient of gravity anomaly

decoupling zone. Further, the location and mean depth of major thrusts are estimated using the wavelet transform. These results provide a relevant input to the forward modeling of the gravity data to derive the density structure of the crust along the transect.

The transformation of potential field (gravity and magnetic) data to some auxiliary space (such as Fourier domain) gives information about the causative sources (Spector and Grant, 1970). Power spectrum analysis (Bhattacharyya, 1966; Dimri, 1992; Blakely, 1995) estimates the mean depth of the interfaces considering the log of power of the Bouguer gravity spectrum as a function of wavenumber/frequency assuming uncorrelated distribution of sources (Spector and Grant, 1970) or scaling nature of sources (Pilkington *et al.*, 1994; Maus and Dimri, 1994, 1995, 1996). The spectrum of gravity anomaly due to a layered source is separated into multiple segments in the frequency domain that can be interpreted in terms of mean depth of the interface. The half of the slope of the segments gives the mean depth of the interfaces following the relationship

$$\ln P(k) = -2kd \qquad (1)$$

where $P(k)$ is the power spectrum, k is the wavenumber, and d is the mean depth of the interfaces to be estimated.

Among various spectral analysis methods, the multitaper method is a high-resolution and superior technique (Percival and Walden, 1993) in comparison to the fast Fourier transform (FFT) method and maximum entropy method for estimating the mean depth of the interfaces from gravity data (Bansal *et al.,* 2006). Here, the multitaper method is applied to the Bouguer anomaly data across the NW Himalaya. The plot of log power spectrum of Bouguer anomaly versus wavenumber (Fig. 3) can be interpreted by the existence of four linear slope segments that are used to derive the mean depth of interfaces as 67.6, 33.9, 11.5 and 1.7 km. The 67.6-km interface corresponds to the Moho depth as observed in other studies across the Himalaya (Rai *et al.*, 2006; Hauck

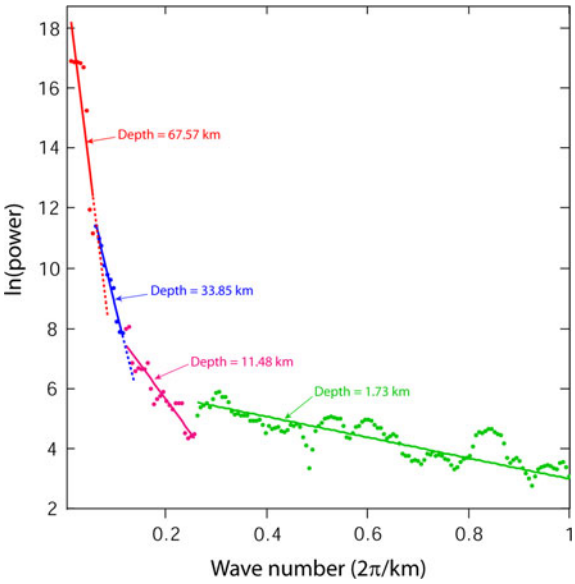

Figure 3
Power spectrum showing log of power of Bouguer gravity spectrum as a function of wavenumber giving the fitted linear segments corresponding to ~67.6, 33.9, 11.5 and 1.7-km depth of interfaces

et al., 1998). The interface at 33.9-km depth can be interpreted as the interface between the upper and lower crusts. The interface at 11.5 km corresponds to the Himalayan decollement thrust. The shallow interface (1.7 km) lies within the relative relief of the profile and is not significant for modeling.

The isostatic response function is calculated for gravity and topography data. In cases where there is both surface and subsurface loading of the lithosphere, the admittance method gives biased results (Forsyth, 1985). However, in tectonically active regions like the Himalaya, subsurface loads cannot be neglected. Therefore, the coherence method is applied to the topography and Bouguer anomaly data. The flexural rigidity (D) of the elastic plate is derived using the relationship

$$D = ET_e^3/12\left(1-v^2\right) \tag{2}$$

where E is Young's modulus (1.1×10^{11}), v is Poisson's ratio (0.25), and T_e is effective elastic thickness.

Predicted coherence function (Fig. 4a) is calculated assuming surface and subsurface loading as independent processes (Forsyth, 1985) with a loading ratio equal to 1, density of the plate equal to 2.67 g/cm^3 and density below the lower compensating boundary as 3.30 g/cm^3. The observed coherence function can be obtained using the relationship:

$$\hat{\gamma}_0^2(k) = \frac{|P_{hb}(k)|^2}{P_{hh}(k)P_{bb}(k)} \tag{3}$$

where $P_{hb}(k)$ is the cross power spectrum of the topography and the Bouguer gravity anomaly in wavenumber domain, and $P_{hh}(k)$ and $P_{bb}(k)$ are the autopower spectrum of the topography and the Bouguer anomaly, respectively.

Further, an unbiased estimate (Munk and Cartwright, 1966) can be given by the relationship:

$$\gamma^2 = (n\gamma_0^2 - 1)/(n-1) \tag{4}$$

where n is the number of independent Fourier coefficients. A least square fit between the observed and predicted coherence function is carried out for T_e = 20–50 km, and the value of the root mean square (RMS) error is the minimum (the best fit) for T_e = 31 km (Fig. 4a inset). The range of uncertainty in the estimated value of T_e can be calculated using the penalty function H^f (McKenzie and Fairhead, 1997), which is defined as:

$$H^f = \left[\frac{1}{N}\sum\left(\frac{C_o - C_p}{\Delta C_o}\right)^2\right]^{1/2} \tag{5}$$

where N is the number of wavenumber bands used, C_o and C_p are observed and predicted coherence, and ΔC_o is standard deviation of C_o. H^f is computed over different values of T_e from 5 to 125 km (Fig. 4b). The minimum value of H^f is 0.33 for T_e equal to 31 km. The range of uncertainty can be given by the two values of T_e corresponding to $2H^f_{min}$. The range of T_e calculated is 18–57 km with a corresponding range of flexural rigidity between 5.70×10^{22} and 1.81×10^{24} N m. To check the consistency of the estimated value, the approach of Simons *et al.* (2003) is followed to calculate the T_e for a more comprehensive layered model with loads on intermediate interfaces and Moho based. The load fractions are considered such that half of the load is on the uppermost interface, and the remaining load is distributed variably on lower interfaces. Again, the minimum value of the penalty function is used for variable load fractions at lower interfaces for different

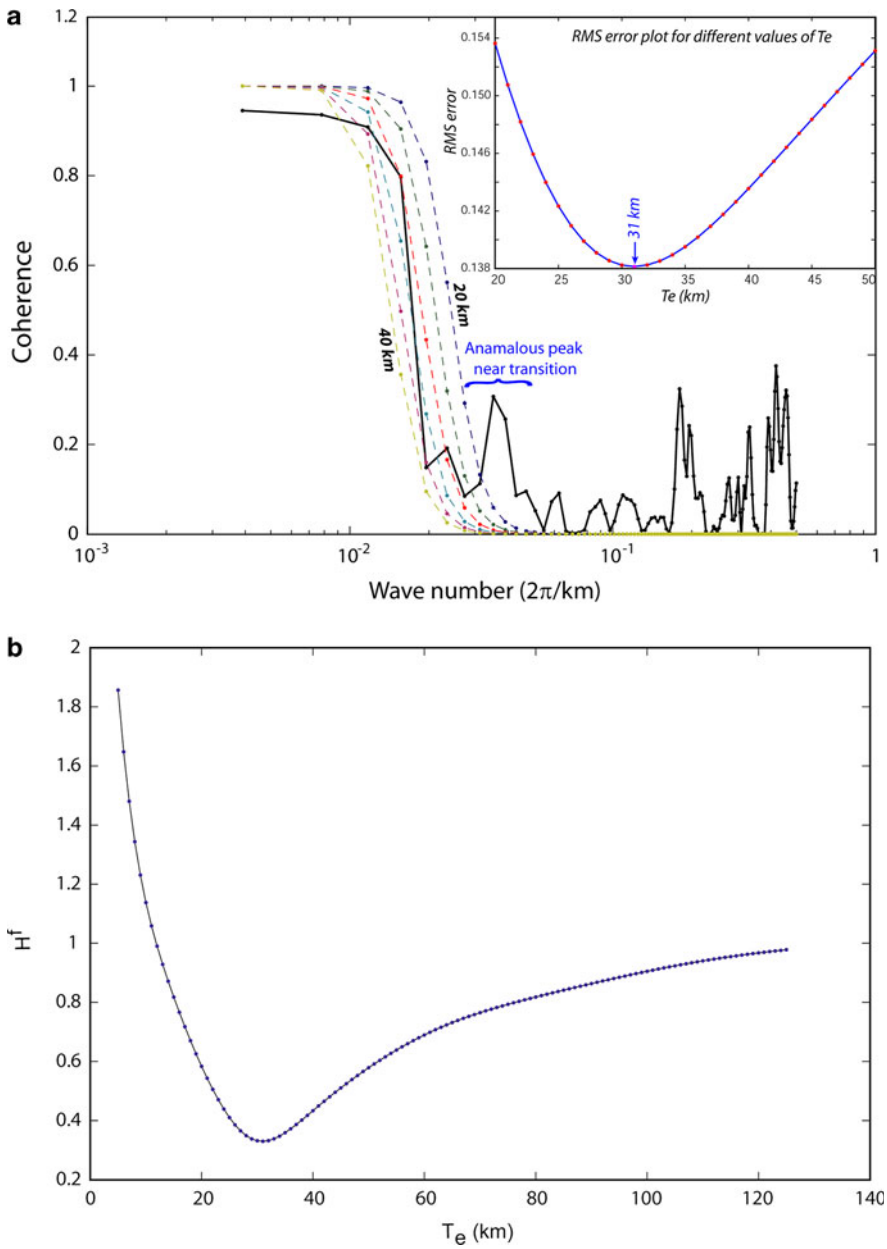

Figure 4

a Observed and predicted coherence function and the RMS error of fitting between these showing $T_e \sim 31$ km. Deviation of observed coherence function from the predicted one in some wavenumber bands is possibly due to correlated loads or folding. Two dominant wavelengths of 178 and 536 km are observed and interpreted as folding in the crustal layers. At high wavenumbers, some correlated loads or low wavelength folds are also observed. **b** Penalty function showing minima at $T_e \sim 31$ km and uncertainty range from 18 to 57 km

T_e values. The estimated value of T_e is 31 km, which is the same as calculated for the above considered simple model. The range of uncertainty of T_e is 10–58 km for a three-layered model. Although the range of uncertainty is wide, the visual inspection of fitting particularly in the transition zone suggests that T_e values in the close vicinity of 31 km are a good estimate. These results for a three layer case show that the T_e value derived for the simple model with loads on the top and bottom gives a consistent estimate, which has

also been observed in previous studies (Bechtel *et al.*, 1987; Caporali, 2000).

The calculated value of flexural rigidity is relatively low. The low value of T_e can be attributed to the crust mantle decoupling and to a substantial loading by surface topography as suggested by Burov and Diament (1992, 1995). The presence of decoupling is further inferred from coherence, admittance and cross spectra. The observed coherence function (Fig. 4a) shows a good correlation of Bouguer gravity and topography at low wavenumber, a transition zone indicating the flexural rigidity of the lithosphere or elastic layer, and low correlation along with an anomalous peak at large wavenumbers. The transition corresponding to flexure begins with a drop of coherence at wavelength $\sim$536 km. An anomalous peak is identified from wavelength 115 to 230 km, centered at wavelength $\sim$178 km. The two wavelengths (178 and 536 km) can be interpreted as two dominant wavelengths of folding for the NW Himalaya due to initial compression. The relative folding of the layers with respect to the surface can be derived by the cross spectra ($P_{hb}(k)$) and admittance ($Q(k)$) in a similar manner as Jin *et al.* (1994) by the equation:

$$Q(k) = \frac{P_{hb}(k)}{P_{hh}(k)} \tag{6}$$

The admittance and cross spectra are positive from wavelength 134 to 268 km (Fig. 5), which show that the wavelength of 178 km is in phase with the surface. The cross spectra is negative for wavelengths >268 km, suggesting that the undulations/foldings of wavelength 536 km are out of phase with the surface. Thus, the spectral behavior of coherence, admittance and cross spectra suggests two wavelengths of 178 and 536 km of folding similar to the results of Burov *et al.* (1993), Jin *et al.* (1994) and Caporali (2000) obtained for other Himalayan regions. These results infer a prominent three-layered structure with a jelly-sandwich type setting (Fig. 6).

The crustal slabs are tectonically stacked in the thrust belt form above the Main Himalayan Thrust, and the density contrast across the tectonic boundaries acts as a source for the Bouguer anomaly. The continuous wavelet transform can be employed to transform the potential field data in the space scale domain (Moreau *et al.,* 1997, 1999; Fedi and Quarta, 1998) without any a priori information. The method shows good resolution and effectively handles the noise and non-stationary nature of potential field data. The technique contributed significant results to several potential field data in different tectonic setups including the gravity data of the Nepal Himalaya (Martelet *et al.,* 2001). Drawing the tectonic analogy in the Himalayan domain, the gravity data from the NW Himalaya are analyzed using the wavelet transform method. The wavelet coefficients are interpreted to delineate the source parameters, mainly the mean depth and location of the litho-tectonic boundaries responsible for the observed Bouguer gravity anomaly.

In the wavelet domain (space scale domain), a signal is decomposed in the orthogonal wavelets of finite duration known as the analyzing wavelet. The convolution product of the analyzing wavelet with a function $\phi_0(x)$ in 2-D physical space gives the continuous wavelet transform (Moreau *et al.,* 1997, 1999) that can be mathematically defined as

$$\begin{aligned} W_{\psi|\phi_0}(b,a) &= \int_{-\infty}^{+\infty} \frac{dx}{a}\psi\left(\frac{b-x}{a}\right)\phi_0(x) \\ &= (D_a\psi * \phi_0)(b) \end{aligned} \tag{7}$$

where ψ is the analyzing wavelet, x is the abscissa along the profile, a is the dilation (scale), b is a position parameter and the dilation operator D_a can be defined as $D_a\psi(x) = \frac{1}{a}g\left(\frac{x}{a}\right)$.

Geological structures like thrusts or a similar discrete body can be approximated by a vertical and inclined step model. Application of the Poisson wavelet as analyzing wavelet gives cone-like patterns in the wavelet domain corresponding to the causative sources of gravity anomaly. The wavelet coefficients along modulus maxima lines drawn on cone-like patterns can be further analyzed for geometry and structure of the causative sources (Sailhac *et al.*, 2000; Martelet *et al.*, 2001). Using real Poisson wavelets, the mean depth and location of causative sources of the potential field data can be calculated by the intersection of modulus maxima lines. For any modulus maxima line, the mean depth can also be estimated by spanning an approximate a priori depth interval for the dilation ranges by a trial and error approach and quantifying the linear character of transformed wavelet coefficients along the modulus

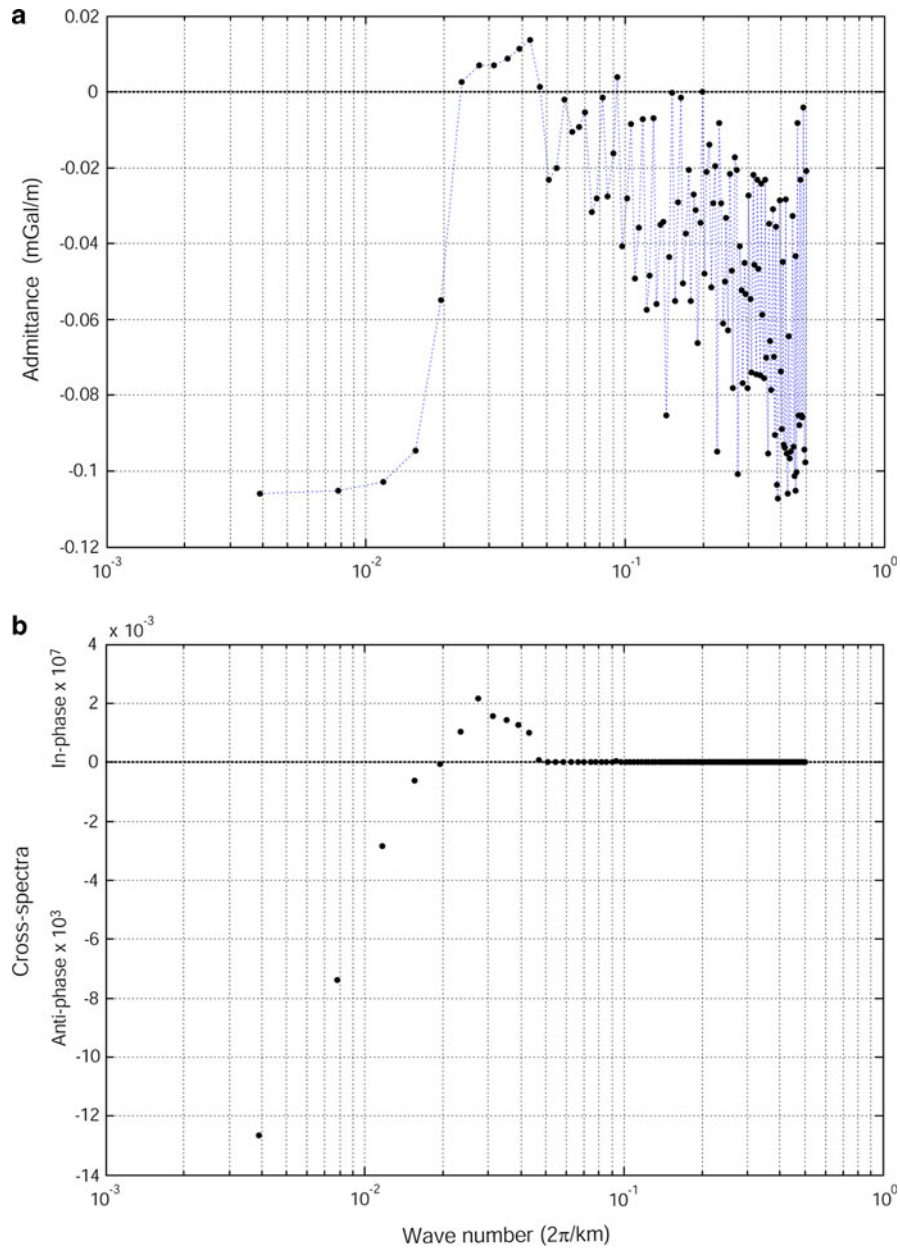

Figure 5
a Admittance and **b** cross spectra between the gravity and topography

maxima line by fitting a polynomial of degree 1. The minima in the misfit curve (in the least square sense) correspond to the mean depth of the source (MOREAU *et al.*, 1999). The slope (β) of the best fitted line for the plot of log ($|Wl/a^{\gamma}$) versus log ($a + z_0$) along any modulus maxima line for different values of z_0 gives information about the structure of the source, where γ is the order of Poisson wavelet used. The slope is equal to -1 for the step model. The wavelet analysis of the synthetic gravity anomaly due to a vertical step using a complex Poisson wavelet is demonstrated to derive the geometry of the source (Fig. 7). The location of the source is just below the modulus maxima line (Fig. 7b). The slope of the fitted straight

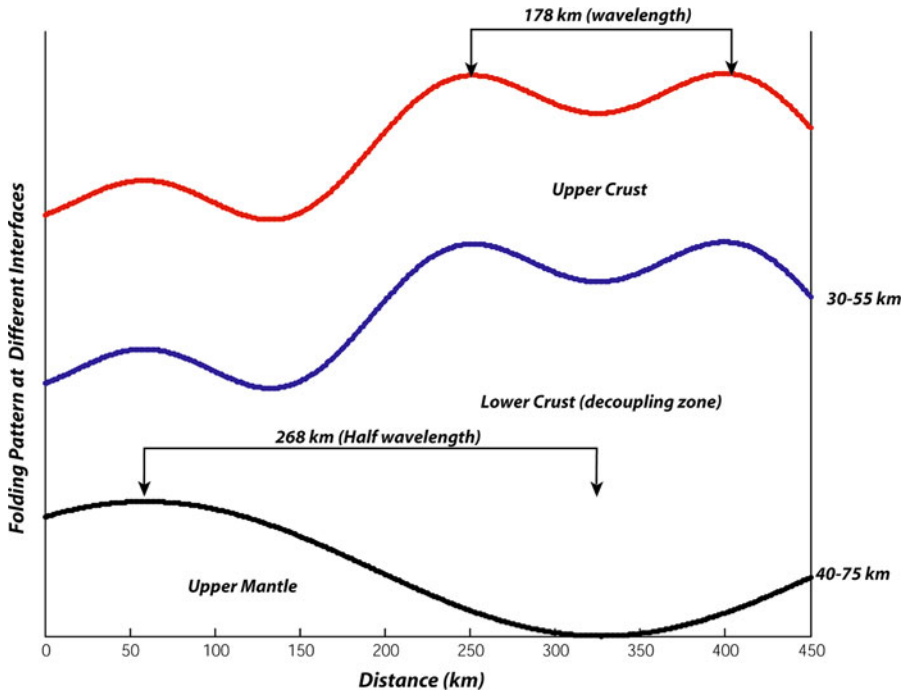

Figure 6
Relative configuration of folded layers due to initial horizontal compression. Moho is undulated by 536-km wavelength fold, whereas topography and Conrad discontinuity show folds at both 178 and 536 km wavelength

line (Fig. 7c) confirms the causative source as a step, and the minima in misfit (Fig. 7d) give the mean depth to the source. Thus, the geometrical properties of modulus maxima lines make it possible to find the location and mean depth of the source. Complex Poisson wavelet is preferred to real wavelet for analyzing the gravity data (Sailhac *et al.,* 2000), though the analysis of both the real and complex wavelet coefficients can improve the confidence of interpretation.

Before applying the continuous wavelet transform, the gravity anomaly is interpolated at an interval of 1.5 km (Fig. 8a) using cubic spline, taking into consideration the edge correction by using the data from the contours of the Bouguer anomaly map (Jin *et al.*, 1994). Then, wavelet coefficients are calculated by continuous wavelet transform using the complex Poisson wavelet of an order of 1 as suggested by Sailhac *et al.* (2000). A number of modulus maxima lines are extracted and the prominent modulus maxima lines (marked by arrows at abscissa, Fig. 8b), which extend to all (low and high) dilations, are considered for further analysis. The distances at which these modulus maxima lines intersect the abscissa yield the location of causative sources. The Bouguer gravity anomaly is now analyzed using the real Poisson wavelet of order 3 (Fig. 8c) showing cone-like structures and modulus maxima lines. The modulus maxima lines calculated using real wavelet, which also give prominent signatures using complex wavelets, are further analyzed (Fig. 8c) to obtain mean depth parameters using negative dilations. The intersection of these extended lines shows the mean depth of the source as D_1–D_9 (Fig. 8c). To check the accuracy of these results using the real wavelet, the wavelet coefficients (Fig. 8b) derived using the complex Poisson wavelet of order 1 are analyzed, and the results for calculation of the structure and its mean depth for D_2 and D_9 modulus maxima lines are shown in Fig. 8d, e, d′, e′. The calculated value of the mean depth is close to the values obtained using the real wavelet of order 3 (Fig. 8c), and the calculated value of β is approximately -1, suggesting the step model (Fig. 8d, d′).

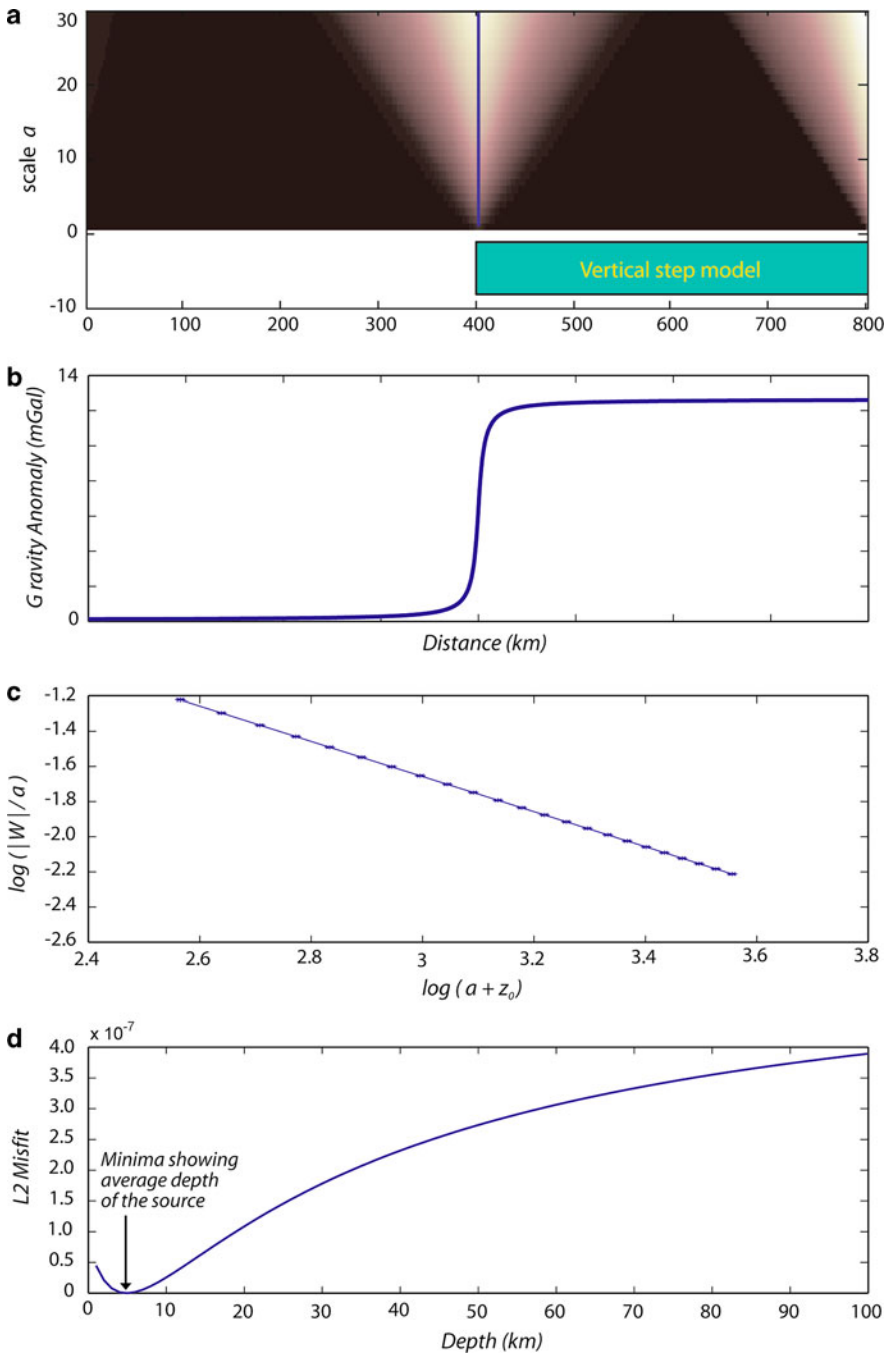

Figure 7

a Wavelet coefficients calculated using a complex Poisson wavelet of an order of $\gamma = 1$. The vertical step model is also shown. The cone structure and the modulus maxima line point towards the location of the vertical step. **b** Synthetic gravity anomaly due to the vertical step. **c** Plot of log ($|W|/a^{\gamma}$) versus log ($a + z_0$) along the modulus maxima line with the best slope of the fitted straight line equal to -1, which shows the shape of the causative body as a step model. **d** Minima misfit curve (in least square sense) showing the plot of misfit versus depth where the minima in the curve give the mean depth of the vertical step as 5 km

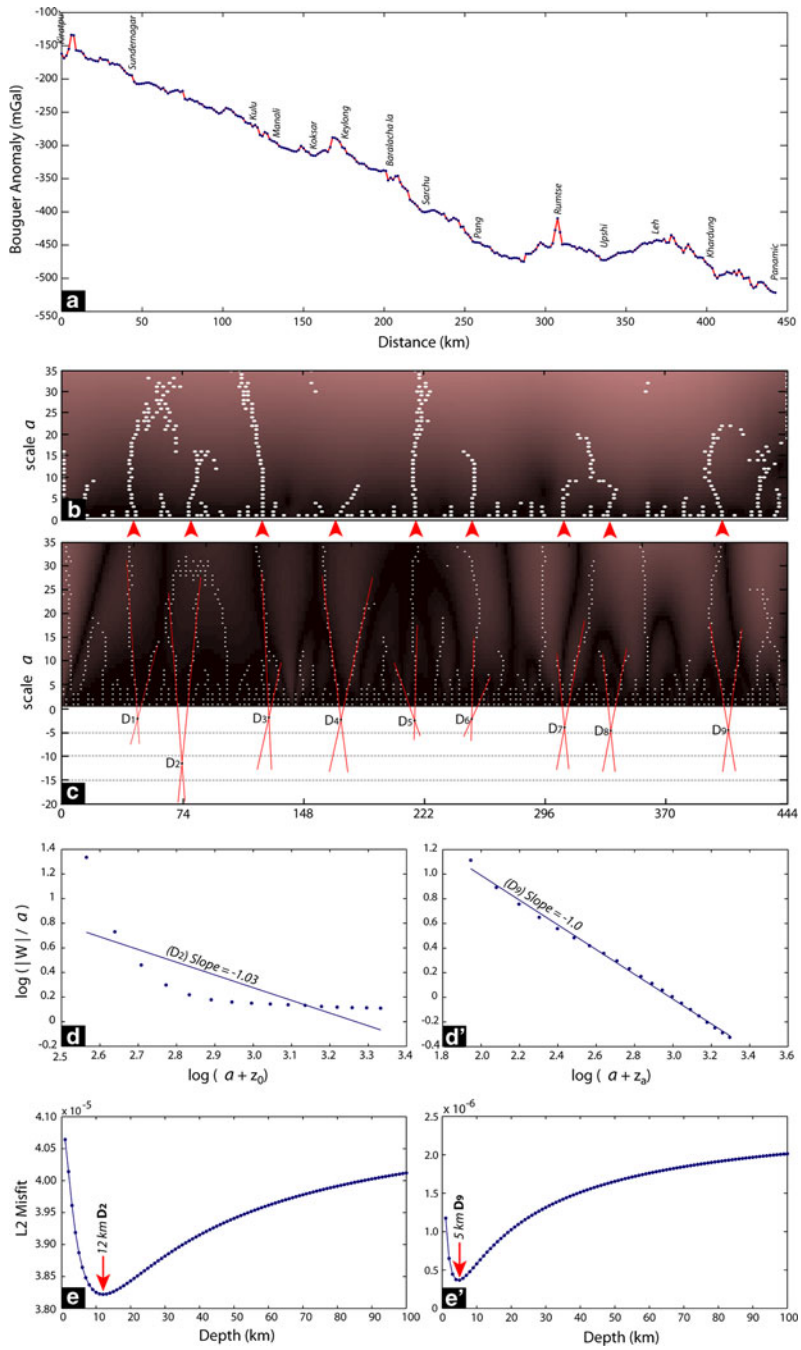

Figure 8

Wavelet analysis of the Bouguer gravity anomaly across the NW Himalaya. **a** Projected Bouguer gravity anomaly interpolated at 1.5 km using cubic spline along the Kiratpur-Manali-Leh-Panamik profile. **b** Wavelet coefficients calculated using the complex Poisson wavelet of order $\gamma = 1$. Major modulus maxima lines are marked by *arrows* at abscissa. **c** Wavelet coefficients calculated using the real Poisson wavelet of order $\gamma = 3$ showing intersections of modulus maxima lines as D_1 to D_9. The negative dilations of D_1 to D_9 correspond to the mean depth of the causative source. **d**, **d′** Plot of log ($|Wl/a^{\gamma}$) versus log ($a + z_0$) along the modulus maxima line with best slope of the fitted straight line showing the structure as a step model ($\beta = -1$). **e**, **e′** Minima misfit curve (in the least square sense) showing a plot of misfit versus depth where minima in the curves give the mean depth as 12 and 5 km for D_2 and D_9, respectively

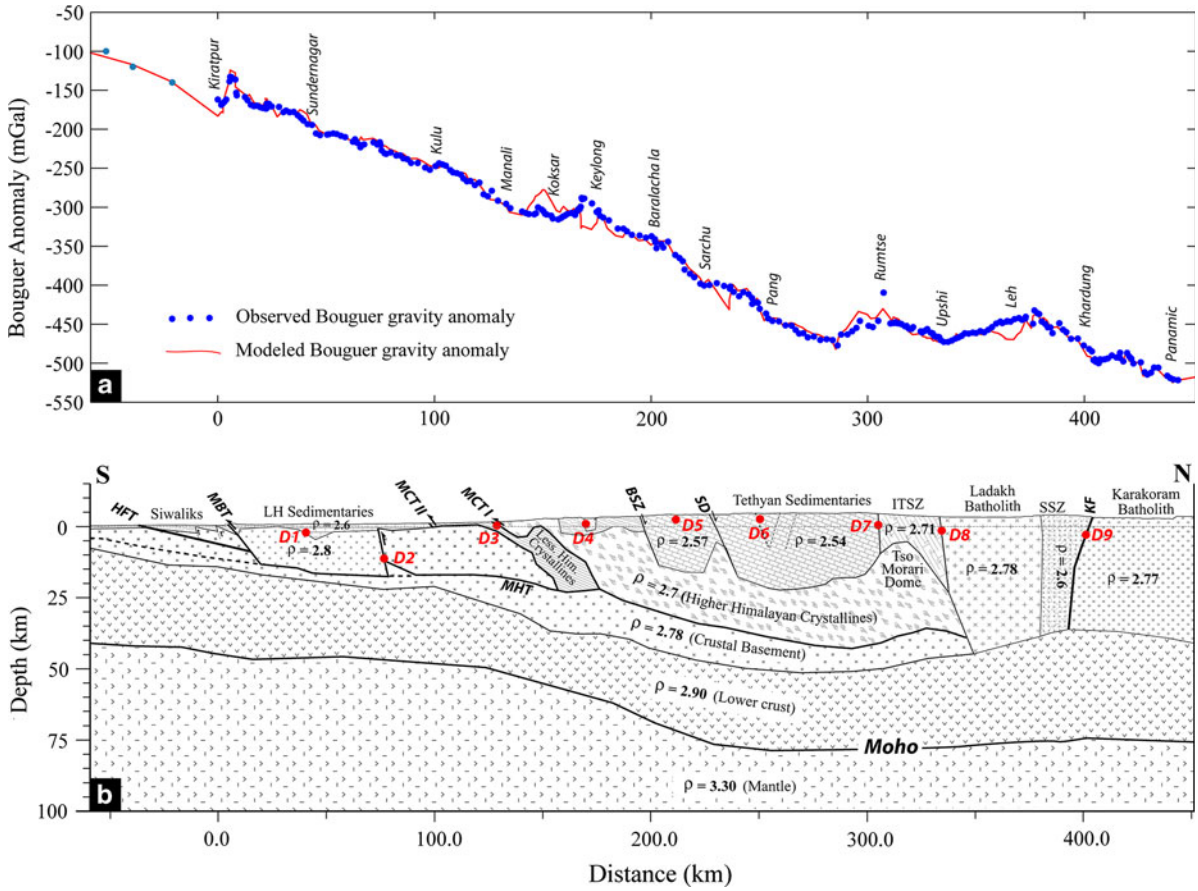

Figure 9

Forward modeling of the Bouguer gravity anomaly across the NW Himalaya incorporating constraints derived from power spectrum analysis, coherence method, wavelet analysis and geological information. **a** Observed and calculated Bouguer gravity anomalies show good correlation with ~9.2% RMS error. The observed data towards the left of the 0 km distance are taken from JIN *et al.* (1994) and modeled to demonstrate the extension of HFT and other layers towards the south. **b** Note the flexure of Moho, the out-of-sequence blind thrust beneath the window zone (D_2) in the Lesser Himalaya, the mid-crustal ramp in the MHT beneath the Higher Himalaya and significant correlation of depths derived by wavelet transform with the structures along the profile in addition to the density structure. (*MHT* Main Himalayan Thrust, *SD* Sarchu Detachment, *KF* Karakoram Fault; other abbreviations are same as in Fig. 1)

3.2. *Forward modeling of the gravity profile*

The observed Bouguer anomaly data are forward modeled to derive a plausible density structure and crustal configuration along the transect. The forward modeling incorporates the topography, geological distribution of litho-tectonic units (Fig. 1b) and average density derived from representative rock samples from different litho-tectonic units (Table 1). The layered configuration of the crust is primarily based on power spectrum analysis results (Fig. 3), which are in agreement with the INDEPTH structures for the central Himalaya (HAUCK *et al.*, 1998). The power spectrum results are substantiated by the Moho configuration along the same transect derived from teleseismic receiver function analysis (RAI *et al.*, 2006). The configuration of the Main Himalayan Thrust for different sections of the transect is based on the previous studies. The retro-deformable cross-sections (POWERS *et al.*, 1998) of the Sub-Himalaya, microseismic studies (THAKUR *et al.*, 2000) and structural constraint on out-of-sequence thrust (PANDEY *et al.*, 2004) for the Lesser Himalaya, magnetotelluric studies (ARORA *et al.*, 2007) and retro-deformable cross-sections (SEARLE, 1986) for the Tethyan Himalaya

and Indus Tsangpo Suture zone are considered. The geometry of the shallow structures is constrained by wavelet analysis (D_1–D_9) (Fig. 8).

The model (Fig. 9) incorporates most of the observable geological parameters along the profile across the NW Himalaya. The geology, structure and basement geometry in the Gangetic plane and Sub-Himalayan region are derived from the ONGC's bore well data and seismic sections (Powers *et al.*, 1998). Part of the gravity profile passes on either side of the oblique ramp of the Main Boundary Thrust in the Kangra reentrant (Fig. 1b), and therefore, it appears as steeper splays in the section (Fig. 9). The basement is further exposed in the antiformal Kulu-Rampur window (Fig. 1b) along an out-of-sequence thrust (Pandey *et al.*, 2003, 2004), which is reflected in the wavelet analysis with D_2 having $\sim$12-km depth (Fig. 9). The Main Central Thrust-I corresponds to a shallow signature (D_3) in the wavelet analysis, suggesting its lesser contribution to the active loading. The variation in the density of Tethyan sediments is attributed to the intense shearing that corresponds to the D_5 and D_6 in wavelet analysis. The contact of the Indus Tsangpo suture zone with the Tethyan sediments and the Ladakh Baholith are reflected as D_7 and D_8 in wavelet analysis, respectively. The volcanics and molasses of the Shyok Suture zone are considered as a wedge that terminates against the Karakoram fault. This is reflected as D_9 in wavelet analysis. The last $\sim$25 km of the section runs parallel to the Karakoram fault without any appreciable change in geology (Fig. 1b) and is accordingly modeled without changing any density structure (Fig. 9). The modeled Bouguer gravity anomaly shows a RMS error of $\sim$9.2% with respect to observed Bouguer anomaly (Fig. 9a).

4. Discussion

The varying degrees of tectonic loading and flexure are imaged by earthquake receiver function analysis (Hetényi *et al.*, 2006; Rai *et al.*, 2006), INDEPTH (Zhao *et al.*, 1993; Hauck *et al.*, 1998) and various other studies (Lyon-Caen and Molnar, 1985; Cattin *et al.*, 2001; Banerjee and Satyaprakash (2003); Jordan and Watts, 2005; Tiwari *et al.*, 2006) in different parts of the Himalaya. Invariably, different studies are in agreement with the three interfaces, the Moho, lower-upper crustal interface (Conrad discontinuity) and mid crustal decollement of the Himalaya (Hetényi *et al.*, 2006). EET is variously discussed in terms of crustal strength vis-à-vis seismicity and the thermo-mechanical behavior of the layered structure beneath the Himalaya (Lyon-Caen and Molnar, 1985; Maggi *et al.*, 2000; Cattin *et al.*, 2001; Jordan and Watts, 2005; Hetényi *et al.*, 2006). The assessment of the flexural rigidity and determination of EET show considerable variation in the Himalayan range (Lyon-Caen and Molnar, 1985; Jordan and Watts, 2005). Deformation models of two strong layers (upper crust and upper mantle) separated by a weak decoupling zone of lower crust when subjected to horizontal compression show folds of two dominant wavelengths (Zuber, 1987; Burov *et al.*, 1993; Burg, 1994). The identification of two anomalous zones at wavelengths 178 and 536 km derived from coherence, admittance and cross spectra indicates folding because of the initial stages of compression (Fig. 6). These results are similar to previous studies of the central Himalaya (Jin *et al.*, 1994) and western Himalaya (Caporali, 2000), and demonstrate folding as a large-scale process in the Himalaya that is related to the crustal thickening. The calculated first order wavelength of 536 km folds all layers, i.e., the upper crust, lower crust and upper mantle, whereas the 178-km wavelength undulations are superposed on the upper crust only. The negative correlation of the 536-km undulations with the surface show an 'inverse boundage' style of folding as suggested by Jin *et al.* (1994) for Tibet. The experiments on rock deformation and models for thermo-mechanical strength of the lithosphere suggest that the strength of the upper crust depends on frictional sliding along thrusts and the crust becoming strong with increasing overburden pressure to a depth of 15 km, which also defines the threshold for ductile creep of quartz-diabase (Burov *et al.*, 1993). Between depths of 25–30 km and the base of the crust, a weak ductile zone should exist, and the thickness of the zone depends on the thickness of the crust (Jin *et al.*, 1994). The weak lower crust facilitates decoupling in the lithosphere and is responsible for the growth of

folding of two distinct wavelengths at different levels in the crust when subjected to lateral compression as suggested by Zuber (1987). The uppermost mantle below the crust remains strong owing to the higher compressive strength of olivine (Ranalli, 1995). The depth interfaces on the basis of the thermo-mechanical property in the lithosphere matches well with the one obtained by spectral analysis and their deformation response to the lateral compression for the NW Himalayan crust. The first order wavelength of folding (536 km in the present case) is four times the total thickness of two strong layers and the intermediate ductile layer, and the second order wavelength (178 km in present case) is four times the thickness of the upper strong layer (Burg, 1994; Jin *et al.*, 1994). Thus, the predicted thickness of the upper crust is around 45 km, and the depth to the base of the upper mantle is around 134 km. The thickness of the upper crust is more or less a good estimate, which is also observed in the model derived by gravity modeling. If we consider the average Moho depth near 68 km based on power spectrum estimates and gravity modeling, the average thicknesses of the ductile layer and upper mantle are around 23 and 66 km, respectively. The value of T_e (31 km), calculated using the coherence method, is likely an underestimate of the true elastic thickness in the presence of the decoupling zone and correlated loads, as also observed in other studies (Jin *et al.*, 1994; Macario *et al.*, 1995; Caporali, 2000). The average T_e of $\sim$31 km (Fig. 4) is consistent with the range for the western Himalaya in Pakistan (Duroy *et al.*, 1989) and western Himalaya and foredeep (Jordan and Watts, 2005).

In interpreting the gravity response of the structures, the wavelet analysis (Fig. 8) delineated the location, mean depth and shape of the source for potential field data (Martelet *et al.*, 2001). The mean depth of the sources of the Bouguer anomaly (Figs. 8c, e, e′) from the major modulus maxima lines (Fig. 8b) are in correlation with the geological structures along the profile (Fig. 9). The results highlight the effectiveness of the technique in a complex tectonic scenario like the Himalaya. However, the methodology has limitations in resolving the causative sources, where the interference of modulus maxima lines is pronounced, especially in the real data. The model derived from forward modeling of the gravity data (Fig. 9b) shows a sub-surface scenario of different litho-tectonic units and Moho configuration, which correspond well with the other studies in the same region. The model suggests a shallower Moho (40–45 km) beneath the Gangetic alluvium. Moho beyond the Lesser Himalaya increases and attains 80-km depth beneath the Tethyan sediments (Fig. 9), suggesting a locus of flexural loading on the Indian crust beneath the Higher Himalaya. The receiver function analysis along the same profile (Rai *et al.*, 2006) also suggests a similar trend. The Moho geometry in the Gangetic alluvium may correspond to the crustal upwarping by flexural bulge in the leading edge of the Indian plate, which is geomorphically observed as the Delhi-Sargodha ridge with very little fluvial cover. Further, the southern part of the profile with the oblique ramp of the Main Boundary Thrust in the Kangra reentrant is the locus of interaction of transverse peninsular tectonic elements with the Himalaya. The microseismicity recorded in the Chamba Nappe region (Fig. 1) reveals that it is confined within 30 km of the crust, and the majority of events are concentrated within a depth range of 5–18 km, and focii lie between 12 and 18 km, defining the Main Himalayan Thrust (Thakur *et al.*, 2000). The velocity structure on the basis of earthquakes in conjunction with microseismicity is interpreted to constrain the depth of decollement at around 15–18 km in the Lesser Himalayan zone (Thakur *et al.*, 2000). The 11.5-km-depth interface (Fig. 3) derived from the power spectrum of the gravity data conservatively correlates with the Main Himalayan Thrust, which is at a depth of 6–7 km in the Sub-Himalaya (Powers *et al.,* 1998) and steepens to 15–18-km depth in the Lesser Himalayan zone (Thakur *et al.*, 2000). Wavelet analysis also yielded a fault structure with a mean depth of $\sim$12 km (D_2) in the window zone of the Lesser Himalaya (Figs. 8, 9). This location and depth coincide well with the mid-crustal ramp modeled to be the locus of strain release in the Himalaya (Yeats and Thakur, 1998). The mid-crustal ramp in the region is observed as an out-of-sequence thrust in the Kulu-Rampur window (Pandey *et al.*, 2003, 2004; Fig. 1) and is inferred in the Nepal Himalaya as the locus of active tectonic loading (Wobus *et al.*, 2006). The gravity responses of the Tso-Morari crystalline and Ladakh batholith with

Indus Tsangpo suture zone rocks are well manifested in a bell-shaped anomaly (Fig. 9). This is compensated by a deeper and steeper under-thrusting of Tso-Morari crystalline beneath the Indus Tsangpo suture zone and upwarping of the upper crust beneath the Ladakh batholith (Fig. 9). The presence of eclogite suggests obduction from a deeper level, and thereby a deeper structure demarcates the northern margin (Fig. 9). These mid-crustal undulations are observed in magnetotelluric studies (Arora *et al.*, 2007) and correspond well with the shorter wavelength out-of-phase folds in the lithosphere.

5. Conclusions

The power spectrum of the Bouguer anomaly indicates a three-layered structure in the lithosphere with a mean depth of interfaces at 11, 34 and 68 km, corresponding to the Main Himalayan Thrust, Conrad discontinuity and Moho, respectively. The average estimate of the T_e value calculated using the coherence method is 31 km. The coherence function shows some anomalous values that differ from the theoretical values of the elastic plate model in some wavelength bands, which is also observed in the admittance and cross-spectra plots. The two dominant wavelengths are explained by folding of the layers, the folds having wavelengths of 178 and 536 km. We interpret that they were developed due to initial horizontal compression and support the concept of large-scale lithospheric folding, which is also reported in the western Himalaya (Caporali, 2000) and Tibet (Jin *et al.*, 1994). The lithospheric folding is explained by the existence of a weak decoupling layer between the upper crust and the upper mantle. The geometry of the major thrusts along the transect derived by wavelet analysis correlates well with the field geological observations. This is incorporated in the forward modeling, and a density structure for the NW Himalaya is proposed (Fig. 9).

Acknowledgments

We thank the anonymous reviewers for the thorough suggestions, which improved the manuscript to the present form. PB acknowledges funding from DST, New Delhi, which enabled the field data generation in the NW Himalaya. We thank Dr. F.J. Simons for the discussion on the computer code for elastic thickness estimation. The conversations about various issues of gravity data with Drs. D.C. Mishra, A.R. Bansal, V.M. Tiwari, Uma Shankar and on Himalayan tectonics with Dr. V.C. Thakur are gratefully acknowledged.

References

Arora, B. R., Unsworth, M. J., and Rawat, G. (2007), *Deep resistivity structure of the northwest Indian Himalaya and its tectonic implications*, Geophys Res Lett *34*, L04307(1–4). doi: 10.1029/2006GL029165

Banerjee, P. and Satyaprakash, (2003), *Crustal configuration in northwestern Himalaya from gravity measurements along Kiratpur-Leh-Panamik Transect*, J Geol Soc India *61*, 529–539

Bansal, A. R., Dimri, V. P., and Sagar, G. V. (2006), *Depth estimation from gravity data using the maximum entropy method (MEM) and the multi taper method (MTM)*, Pure Appl Geophys *163*(7), 1417–1434

Bechtel, T. D., Forsyth, D. W., and Swain, C. J. (1987), *Mechanisms of isostatic compensation in the vicinity of the East African Rift, Kenya*, Geophys J R Astron Soc *90*, 445–465

Bhattacharyya, B. K. (1966), *Continuous spectrum of the total-magnetic-field anomaly due to a rectangular prismatic body*, Geophysics *31*(1), 97–121

Blakely, R. J., *Potential Theory in Gravity and Magnetic Applications* (Cambridge University Press, New York 1995)

Burg, J. P. (1994), *Shortening of analogue models of the continental lithosphere: New hypothesis for the formation of the Tibetan plateau*, Tectonics *13*, 475–483

Burov, E. B., and Diament, M. (1992), *Flexure of the continental lithosphere with multilayered rheology*, Geophys J Int *109*, 449–468

Burov, E. B., and Diament, M. (1995), *The effective elastic thickness (Te) of continental lithosphere: what does it really mean*? J Geophys Res *100*, 3905–3927

Burov, E. B., and Watts, A. B. (2006), *The long-term strength of the continental lithosphere: "jelly sandwich' or 'crème brûlée"?*, GSA Today *16*(1), 4–10

Burov, E. B., Lobkovsky, L. I., Cloetingh, S., and Nikishin, A. M. (1993), *Continental lithosphere folding in central Asia, part II,: Constraints from gravity and topography*, Tectonophysics *226*, 73–87

Caporali, A. (2000), *Buckling of the lithosphere in western Himalaya: Constraints from gravity and topography data*, J Geophys Res *105*, 3103–3113

Cattin, R., Martelet, G., Henry, P., Avouac, J. P., Diament, M., and Shakya, T. R. (2001), *Gravity anomalies, crustal structure and thermomechanical support of the Himalaya of Central Nepal*, Geophys J Int. *147*, 381–392

Chamoli, A., Srivastava, R. P. and Dimri, V. P. (2006), *Source depth characterization of potential field data of Bay of Bengal by continuous wavelet transform*, Ind J Mar Sci *35*(3), 195–204

Dimri, V. P., *Deconvolution and inverse theory* (Elsevier Science Publishers, Amsterdam 1992)

Duroy, Y., Farah, A., and Lillie, R. J. (1989), Subsurface densities and lithospheric flexure of the Himalayan foreland in Pakistan, In *Tectonics of western Himalayas: Geol. Soc. Amer. Sp. Paper,* (eds. Malinconico L. L., and Lillie R. J.), vol 132, pp 217–236

Fedi, M., and Quarta, T. (1998), *Wavelet analysis for the regional-residual and local separation of potential field anomalies*, Geophys Prosp 46, 507–525.

Forsyth, D. W. (1985), *Subsurface loading and estimates of the flexural rigidity of continental lithosphere,* J Geophys Res *90*(B14), 12,623–12,632

Gansser, A., *Geology of the Himalayas* (John Wiley, London 1964)

Hauck, M. L., Nelson, K. D., Brown, L. D., Zhao, W., and Ross, A. R. (1998), *Crustal structure of the Himalaya orogen at ~90 east longitude from INDEPTH deep reflection profiles*, Tectonics 17, 481–500

Hetényi, G, Cattin, R., Vergne, J., and Nábělek, J. L. (2006), *The effective elastic thickness of the Indian plate from receiver function imaging, gravity anomalies and thermomechanical modeling*, Geophys J Int *167*, 1106–1118. doi:10.1111/j.1365-246X.2006.03198.x.

Hornby, P., Boschetti, F., and Horowitz, F. G. (1999), *Analysis of potential field data in the wavelet domain*, Geophys J Int *137*, 175–196

Jin, Y., McNutt, M. K., and Zhu, Y. (1994), *Evidence from gravity and topography data for folding of Tibet*, Nature *371*, 669–674.

Jordan, T. A., and Watts, A. B. (2005), *Gravity anomalies, flexure and the elastic thickness structure of the India-Eurasia collision system*, Earth Planet Sci Lett *236*, 732–750

Lyon-Caen, H., and Molnar, P. (1983), *Constraints on the structure of the Himalaya from an analysis of gravity anomalies and a flexural model of the lithosphere*, J Geophys Res *88*, 8171–8191

Lyon-Caen, H., and Molnar, P. (1985), *Gravity anomalies, flexure of the Indian plate and the structure, support and evolution of the Himalaya and Ganga Basin*, Tectonics *4*, 513–538

Macario, A., Malinverno, A., and Haxby, W. F. (1995), *On the robustness of the elastic thickness estimates obtained using the coherence method*, J Geophys Res *100*(B8), 15,163–15,172

Maggi, A., Jackson, J. A., McKenzie, D., and Priestley, K. (2000), *Earthquake focal depths, effective elastic thickness, and the strength of the continental lithosphere*, Geology 28, 495–498

Martelet, G., Sailhac, P., Moreau, F., and Diament, M. (2001), *Characterization of geological boundaries using 1-D wavelet transform on gravity data: Theory and application to the Himalaya*, Geophysics *66*, 1116–1129

Maus, S., and Dimri, V. P. (1994), *Scaling properties of potential fields due to scaling sources*, Geophys Res Lett *21*, 891–894

Maus, S., and Dimri, V. P. (1995), *Potential field power spectrum inversion for scaling geology*, J Geophys Res *100*, 12605–12616

Maus, S., and Dimri, V. P. (1996), *Depth estimation from the scaling power spectrum of potential field?*, Geophys J Int *124*, 113–120

McKenzie, D., and Fairhead, D. (1997), *Estimates of the effective elastic thickness of the continental lithosphere from Bouguer and free air gravity anomalies*, J Geophys Res *102*, 27523–27552

Moreau, F., Gibert, D., Holschneider, M., and Saracco, G. (1997), *Wavelet analysis of potential fields*, Inverse Probl *23*, 165–178

Moreau, F., Gibert, D., Holschneider, M., and Saracco, G. (1999), *Identification of sources of potential fields with continuous wavelet transform: Basic theory,* J Geophys Res *104*, 5003–5013

Munk, W. H., and Cartwright, D. E. (1966), *Tidal spectroscopy and prediction*, Philos Trans R Soc Lond Ser A *259*, 533–581

Pandey, A. K., Virdi, N. S., and Gairola, V. K. (2003), *Evolution of structural fabrics and deformation events in the Kulu-Rampur and Larji Window zones, NW Himalaya, India*, Himalayan Geol *24*(1), 1–21

Pandey, A. K., Sachan, H. K., and Virdi, N. S. (2004), *Exhumation history of a shear zone constrained by microstructural and fluid inclusion techniques: example from the Satluj Valley, NW Himalaya India*, J Asian Earth Sci *23*, 391–406

Percival, D. B., and Walden, A. T., *Spectral Analysis for Physical Applications: Multitaper and Conventional Univariate Techniques* (Cambridge University Press 1993)

Pilkington, M., Gregotski, M. E., and Todoeschuck, J. P. (1994), *Using fractal crust magnetization models in magnetic interpretation*, Geophys Prospect *42*, 677–692

Powers, P. M., Lillie, R. J., and Yeats, R. S. (1998), *Structure and shortening of the Kangra and Dehra Dun reentrants, Sub-Himalaya, India*, GSA Bull 110(8),1010–1027

Rai, S. S., Priestley, K., Gaur, V. K., Mitra, S., Singh, M. P., and Searle, M. (2006), *Configuration of the Indian Moho beneath the NW Himalaya and Ladakh*, Geophys Res Lett *33*, L15308(1–5). doi:10.1029/2006GL026076.

Ranalli, G., *Rheology of the Earth*, 2nd edn (Chapman & Hall, London, 1995)

Sailhac, P., Galdeno, A., Gibert, D., and Moreau, F. (2000), *Identification of sources of potential fields with the continuous wavelet transform: Complex wavelets and application to aeromagnetic profiles in French Guiana*, J Geophys Res 105, 19,455–19,475

Searle, M. P. (1986), *Structural evolution and sequence of thrusting in the High Himalayan, Tibetan-Tethys and Indus suture zones of Zanskar and Ladakh, Western Himalaya*, J Struct Geol 8, 923–936.

Simons, F. J., van der Hilst, R. D., and Zuber, M. T. (2003), Spatio-spectral localization of isostatic coherence anisotropy in Australia and its relation to seismic anisotropy: Implications for lithospheric deformation, J Geophys Res *108*(B5), 2250. doi: 10.1029/2001JB000704.

Spector, A., and Grant, F. S. (1970), *Statistical models for interpreting aeromagnetic data*, Geophysics 35, 293–302

Srikantia, S. V., and Bhargava, O. N., *Geology of Himachal Pradesh* (Geological Society of India Publications, India 1998)

Thakur, V. C., *Geology of Western Himalaya* (Pergamon Press, Oxford 1992)

Thakur, V. C., Sriram, V., and Mundepi, A. K. (2000), *Seismotectonics of the great 1905 Kangra earthquake meizoseismal region in Kangra–Chamba, NW Himalaya*, Tectonophysics *326*, 289–298

Tiwari, V. M., Rao, M. B. S. V., Mishra, D. C., and Singh, B. (2006), *Crustal structure across Sikkim, NE Himalaya from new gravity and magnetic data*, Earth Planet Sci Lett *247*, 61–69

Valdiya, K. S. (1980), The two intracrustal boundary thrusts of the Himalaya, Tectonophysics *662*, 323–348

Wobus, C. W., Whipple, K. X., and Hodges, K. V. (2006), *Neotectonics of the central Nepalese Himalaya: Constrains from geomorphology, detrital $^{40}Ar/^{39}Ar$ thermochronology and the thermal modeling*, Tectonics 25, TC4011(1–18). doi:10.1029/2005TC001935.

YEATS, R. S., and THAKUR, V. C. (1998), Reassessment of earthquake hazard based on a fault-bend fold model of the Himalayan-plate boundary fault, Curr Sci *74*, 230–233

ZHAO, W., NELSON, K. D., and the Project INDEPTH Team (J. CHE, J. GUO, D. LU, C. WU, X. LIU, L. D. BROWN, M. L. HAUCK, J. T. KUO, S. L. KLEMPERER, Y. MAKOVSKY) (1993), *Deep Seismic-reflection Evidence for Continental Under-thrusting beneath Southern Tibet*, Nature 366, 557–559

ZUBER, M. (1987), *Constraints on the lithospheric structure of venus from mechanical models and tectonic surface features*, J Geophys Res *92*(B4), E541–E551

(Received July 14, 2008, revised April 1, 2010, accepted April 5, 2010, Published online May 18, 2010)